The Acoustics of Earth Materials- Geohazard Forecasting

Aditya Advani
Haverford College Department of Physics and Astronomy, Class of 2024
(Dated: May 29, 2024)

We discuss techniques and develop instrumentation used to measure the Vibrational Density of Modes of disordered, athermal materials. An excess of low-frequency (floppy) modes when compared with Debye scaling is associated with the liquid/disordered solid transition (jamming). In this paper, we construct a system to apply constant compressive strain and acoustic perturbation to a granular sample, whose particle velocites are then measured using piezoelectric ceramics. We then use We then use Dickey's (1969) methods (see Section 6.5), previously applied in thermal systems, to calculate the Vibrational Density of Modes of a disordered sample using a velocity autocorrelation. Changes in low frequency features (like peaks) in the Vibrational Density of Modes before, during, and after perturbing the sample might correlate with a loss of rigidity in granular structure and aid geohazard forecasting techniques.

Keywords: Density of Modes, Geohazard Forecasting, Boson Peak, Granular Failure, Jamming Transition, Instrumentation.

1. OVERVIEW

Our world is full of disordered materials. From cereal in a bowl to traffic jams, disordered move in chaotic ways. These systems can be hard to predict and understand because at a first glance it is difficult to see the patterns in how they behave. Some instances of granular unpredictability can be quite harmless, how grains of cereal behave when we enjoy them with a cold bowl of milk, but failure of granular solids can cause earthquakes and landslides that result in huge losses of human life and infrastructure every year. This paper aims to use the Density of Modes of granular matter to forecast such geohazards which impact millions of lives every year.

In 1998, Liu and Nagel [1] hypothesized that all sorts of disordered solids could be described using a phase diagram (Figure 1) featuring a phase transition, dubbed "Jamming". In this phase diagram, Liu and Nagel are proposing that a disordered system can jam if the density is high enough. Additionally, when a system is jammed, one can unjam it by either raising the temperature or applying stress. There is a Jamming Transition beyond which disordered materials can fail and return to an unjammed configuration, controlled by packing density, temperature or stress. This paper has since informed multiple different studies leading us to a better understanding of the Jamming Transition in disordered materials. This section provides an overview of a few of these studies which discuss how disordered materials behave differently from traditional solids, liquids and gasses.

Jaeger, Nagel and Behringer [2] further review the "Janssen Effect for granular solids [1]" showing us that even "solid" disordered materials behave in unintuitive ways. If a regular solid were slowly stacked into a pile (say in a tube), the pressure at the bottom would increase indefinitely, but they showed that when a granular material is stacked (in the same tube), the pressure at the bottom increases unto a maximum value that is independent of height (Figure 2).

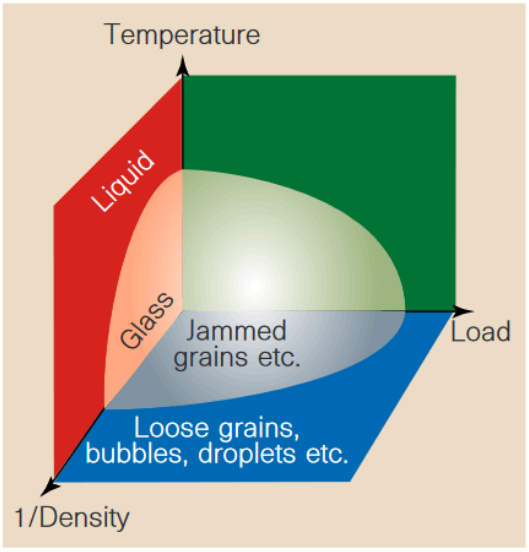

Figure 1: Liu and Nagel [1] propose a possible jamming phase diagram where different granular materials all share similar properties

The distribution of forces in Figure 2(b) was found to fit the following line, where c and f_0 are constant.

$$P(f) = ce^{\frac{f}{f_0}} \tag{1.1}$$

The Janssen Effect is a counter intuitive result that demonstrates how granular matter functions very differently than conventional matter.

In the very same paper, Jaeger, Nagel, and Behringer [3] also describe how granular material flows like a liquid (granular hydrodynamics). Most theories on granular hydrodynamics consist of partial differential equations analogous to Navier Stokes, but with much more complex structure. This is because Navier Stokes equations using an averaging process over length and time scales that

[1] The effect is named after H.A.Jannsen, who made this discovery in the early 19th century.

are much larger than the typical microscopic scales and macroscopic scales we observe in granular flow.

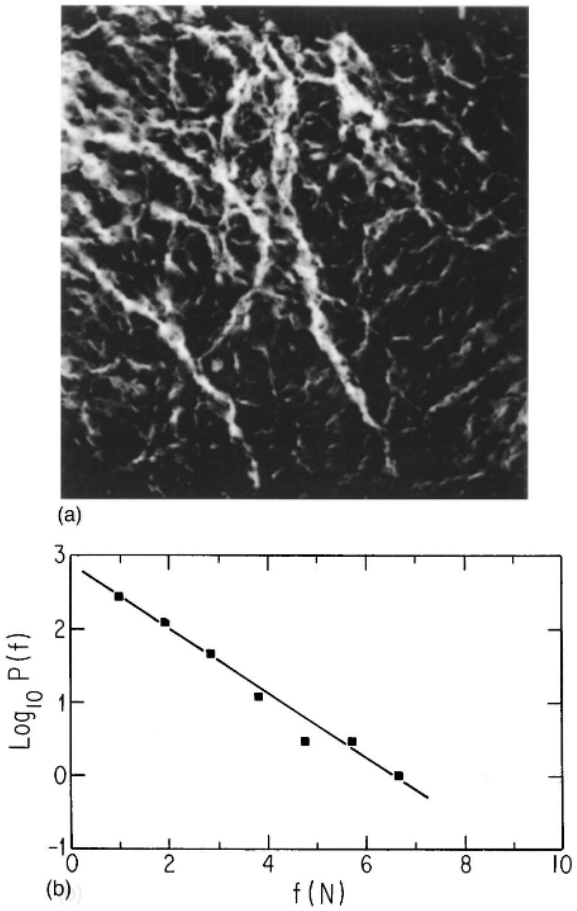

Figure 2: (a) A piece of carbon paper at the bottom of the tube containing granular matter was used to measure the forces on the paper. (b) A log plot of the distribution of force P versus the force f at the bottom of the tube [2].

Convective flow was first observed by Faraday over 180 years ago, but the underlying mechanisms are not well understood. When particles are placed in a configuration like in Figure 3 and vibrated using a sinusoidal driving frequency (vertically) to induce some granular flow, we observe particles in the center moving upward and particles near the side walls moving downwards in a thin stream. Jaeger also showed that the direction of convective flow can be reversed if boundary conditions were changed appropriately.

The other feature of granular hydrodynamics Jaeger observed was granular separation. Larger particles would move to the top and smaller particles would collect at the bottom. This distribution was observed regardless of particle density. Knight (1993) [4] also shows a connection between convective flow and separation in systems that are shaken vertically. Large particles collect at the top due to convective flow but then are unable to return to the bottom via the sides as they are not small enough to slip through the cracks, leaving them stranded at the top. Granular materials, unlike other fluids, can "un-mix" themselves in this way, which is counter-intuitive.

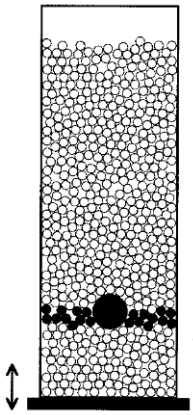

Figure 3: A figure demonstrating Jaeger's experimental setup to observe convective flow and separation [2].

When granular matter collides, it collides inelastically. For example, if we drop one ball on a table, it will bounce back, but a bunch of balls in a bag will land and not bounce because of inelastic collisions between the balls in the bag that dampen the momentum of the system. Jaeger references a simulation (Figure 4) by Goldhirsch and Zanetti [3, p 37] of 40000 colliding particles in a two dimensional plane.

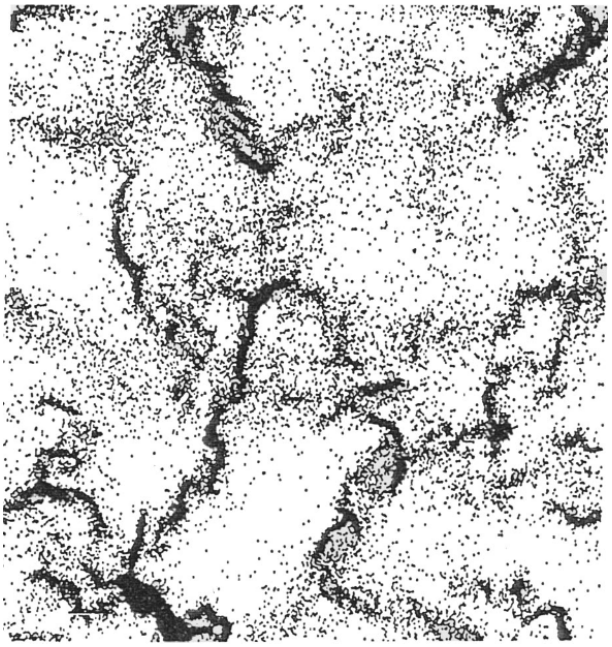

Figure 4: A simulation by Goldhirsch and Zanetti where 40000 particles collide inelastically in 2 dimensions. The coefficient of restitution is 0.6 and the simulation time corresponds to 500 collisions per particle [2].

The presence of clustering in this figure is easy to see. Multiple particles that collide inelastically will cluster together as they eventually settle. This specific type of clustering is referred to as an "inelastic collapse" of the system. It is not well understood why clustering leads to long chains of particles instead of large blobs.

So, we have seen examples of granular solids that do not function like we expect solids to, granular fluids that self unmix themselves using convection and free granular flow that collapses into long clustered chains of particles. Granular matter is not fully understood and that our current theories of solids, liquids and gasses are perhaps too rigid to describe something as disordered as the rich dynamic materials of the earth.

Therefore, much of soft matter since 2000 has been focused on developing techniques to study disordered materials in all their various forms.

2. THE DENSITY OF MODES

The Vibrational Density of Modes $D(\omega)$ (DoM) of a material measures how many modes a material possesses at any given frequency. It is a measure of the different ways a system can respond at any given frequency, and so, it is a function whose purpose is to be integrated. When we integrate a DoM function from some frequency ω_a to ω_b, we should find the number of modes present between those two frequencies.

This section focuses on the math behind the Density of Modes function $D(\omega)$.

2.1. Debye Scaling

In 1912, Peter Debye proposed that we view solids as a "phonon gas". We provide a brief overview of his model and the Density of Modes for a *Debye Solid*.

Debye described phonons as massless quantized vibrations that move through the solid. Each phonon has a specific energy, just like a wave. [5, p 459]

$$\epsilon = hf = \frac{hc_s}{\lambda} \tag{2.1.1}$$

Where λ is the wavelength of the phonon and c_s is its speed. Phonons are bosons as their chemical potential is zero for the same reason as for photons.

Note that since phonons behave like elastic waves in a solid, they must have wavelengths greater than twice the spacing between particles (d). $\lambda \geq 2d$. This is illustrated in Figure 5.

Phonons are different from other gaseous particles because there is a maximum upper limit to their energy (See ϵ_f in Figure 6), called the *Debye Cutoff*. We have have $\lambda \geq 2d$, a lower limit on wavelength which places an upper limit on energy [5].

We know that the motion of one simple harmonic oscillator has a characteristic frequency ω_a. If there are two simple harmonic oscillators, they must have two frequencies, ω_a and ω_b. Then, if there are $3N_a$ states (N_a is the number of particles, and each particle can oscillate in 3 dimensions), we must have $3N_a$ characteristic frequencies. The upper limit is given by [5]:

$$\epsilon_D = hc_s(\frac{3N_a}{4\pi V})^{\frac{1}{3}} = 0.62hc_s(\frac{N_a}{V})^{\frac{1}{3}} \tag{2.1.2}$$

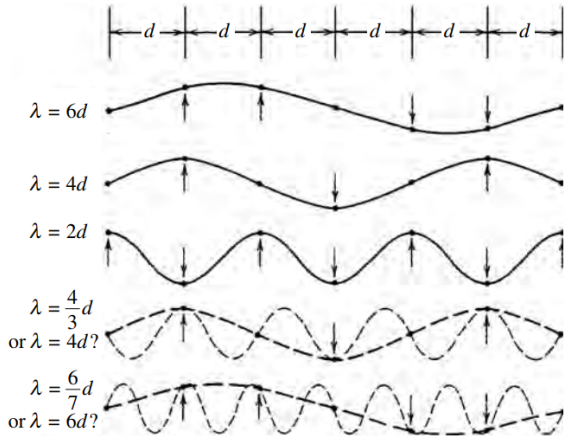

Figure 5: All elastic waves must satisfy $\lambda \geq 2d$. A wave with $\lambda = 6d/7$ is shown to be indistinguishable from a wave with $\lambda = 6d$ in this figure [5, p 459].

It turns out that the Debye cutoff energy is simply a function of the density of atoms $\frac{N_a}{V}$ and phonon speed c_s. Often, we write the cutoff energy (ϵ_D) as a frequency ($h\omega_D$) or a temperature (kT_D). Stowe [5] solves for the distribution of phonons given by: (for $0 \leq \epsilon \leq \epsilon_D$)

$$dN = \frac{9N_a}{\epsilon_D^3}\int_0^{\epsilon_D} \frac{\epsilon^2}{e^{\epsilon\beta} - 1}\, d\epsilon \tag{2.1.3}$$

And the total energy of the Debye system is then given by the sum of the energies of the individual phonons. Note that $D(T)$ (in Equation 2.1.5) is called the Debye function and is not a measurement of the DoM.

$$E = (\frac{9N_a}{\epsilon_D^3})(kT^4)\int_0^{\epsilon_D/KT} \frac{x^3}{e^x - 1}\, dx \tag{2.1.4}$$

$$E = 3N_a kT D(T) \tag{2.1.5}$$

$$D(T) = 3(\frac{kt}{\epsilon_D})^3\int_0^{\epsilon_D/KT} \frac{x^3}{e^x - 1}\, dx \tag{2.1.6}$$

Schroder (1999) [6, p 280] describes the energy of phonons (as quantized vibrational waves):

$$\epsilon = \frac{h^2}{8mL^2}n^2 \tag{2.1.7}$$

$$n = \sqrt{\frac{8mL^2}{h^2}}\sqrt{\epsilon} \tag{2.1.8}$$

$$dn = \sqrt{\frac{8mL^2}{h^2}}\frac{1}{2\sqrt{\epsilon}}d\epsilon \tag{2.1.9}$$

dn can be thought of as the number of singular particles per unit energy.

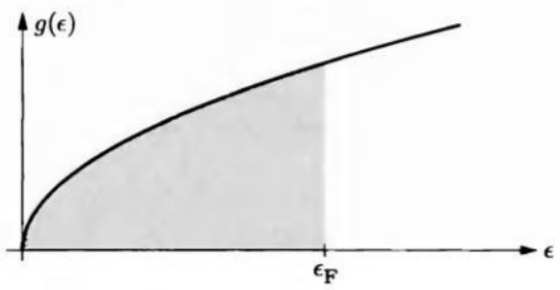

Figure 6: Density of Modes of perfect non-interacting non-relativistic particles in a three dimensional box. [6, p 280] Note that $D(\omega) \sim \omega^{d-1} = \omega^2$. Based on the maximum energy for the system the states below ϵ_f are the occupied states.

So, Schroder sums over all energies times the number of states with that energy, to find an equation for the Density of Modes for a Debye Solid.

$$D(\epsilon) = (\frac{\pi(8m)^{3/2}}{2h^3})V\sqrt{\epsilon} \qquad (2.1.10)$$

Where m is the mass of a particle and V the volume of the solid. In d dimensions, a perfect Debye solid has a Density of Modes $D(\omega) \sim \omega^{d-1}$. Figure 6 is a plot of the DoM of a perfect Debye like Solid.

This model however only describes a perfect Debye solid. In reality, disordered matter differs from Debye scaling in a few ways. It is extremely important to note that $D(\omega) \sim \omega^{d-1}$ only holds for a Debye solid. In the next sections, we will be focused measuring how the DoM in granular systems *differs from* Debye scaling.

2.2. The Density of Modes of granular materials

One of the striking differences between the Density of Modes in Debye solids and disordered solids is that disordered materials disagree with Debye scaling at lower frequencies. In a disordered solid, we observe a plateau in the DoM at lower frequencies (Figure 7) instead of the expected scaling $D(\omega) \sim \omega^{d-1}$. In completely jammed disordered solids, this plateau extends to $\omega = 0$, while in marginally jammed disordered solids, we can see that this plateau begins some critical frequency ω^*. In this section, we aim to explore this anomalous excess in low frequency modes observed in the Density of Modes of granular materials.

Figure 7, a simulation by Xu et al [7] demonstrates this concept. Crystalline materials behave like Debye solids, so Figure 7(b) exhibits Debye scaling. However, Figure 7(a) has a bump of excess low frequency modes.

When we measure the DoM of a disordered material, we often will normalize it by dividing by Debye Scaling, and therefore, we are able to note the frequency ω^* at which the anomalous low frequency modes are peaked. This is the Boson Peak, and it is one of the most important features of the Density of Modes in granular matter (Figure 8).

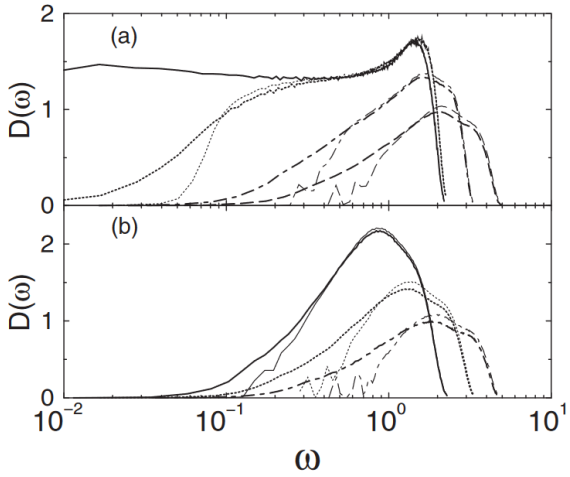

Figure 7: The Density of Modes simulated for 1000 3D glasses over 100 different configurations. [7] (a) Shows the DoM for marginally jammed solids and (b) for unjammed Debye-like solids. Note the excess in low frequency modes.

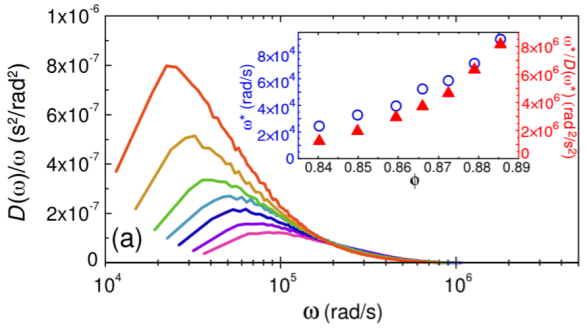

Figure 8: The Density of Modes for a 2D system of colloidal particles normalized to show the boson peak. The system is compressed to different packing fractions to show how ω^* changes with pressure.Note that the red plot is the lowest and the pink plot is the highest packing fraction (and pressure).

2.3. The Boson Peak

The Boson Peak is perhaps the most striking feature of the Density of Modes of disordered materials near the jamming transition. Later, we will present a thermal technique used to measure the characteristic frequency ω^* of the Boson Peak in granular materials.

Chen et al [8] demonstrate the ability to isolate ω^* by normalizing the Density of Modes with respect to Debye Scaling(Figure 8).

In a 2-dimensional system, Chen et al compressed colloidal thermosensitive hydrogel particles and noted the change in the Density of Modes. They normalized the system by dividing $D(\omega)$ by ω^1 so we can clearly see the boson peak and its characteristic frequency ω^*.

Owens et al [9] take this concept further in Figure 9. Their experiment uses piezoelectric ceramics to measure the Density of Modes. Unlike Chen, they also consider a crystalline case to compare the amorphous particles with. Instead of normalizing by dividing by ω^2, they normal-

ize by dividing the amorphous Density of Modes by the crystalline measurement to isolate the boson peak.

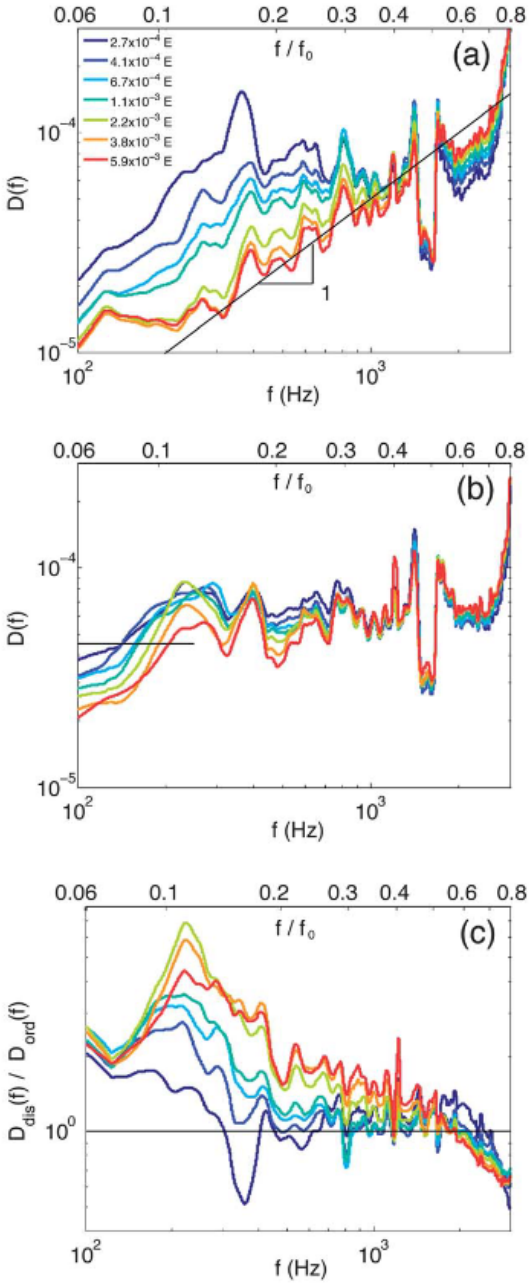

Figure 9: Owens and Daniels [9] measure the Density of Modes for (a) Ordered and (b) Disordered packings and (c) Ratio of ordered packings to disordered packings. The black line in (a) represents Debye Scaling

Since ordered solids are more Debye-like, we see a Boson Peak when we divide the DoM of disordered packings by the ordered packings. Figure 8 is a good example of how the characteristic frequency ω^* for a system changes with pressure. As pressure increases, we observe ω^* increases, but much slower than it does in simulations with frictionless spheres (Shown in Figure 10 for comparison) [10].

Changes in pressure are one of the main factors causing

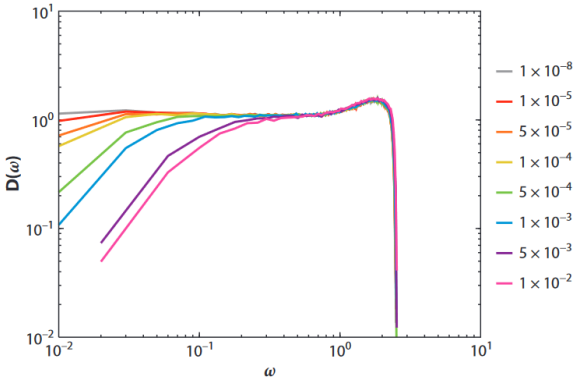

Figure 10: Liu and Nagel [10] measure the Density of Modes for three dimensional ideal sphere packings without friction at various compressions. Their results show a much larger increase in ω^* as pressure increases than Daniels and Owens [9].

ω^* to change. For example, an increase in pressure in the earth might build up to a stick-slip failure event as pressure is released. In this case, we would probably observe ω^* increasing steadily until failure and then dropping back down after a loss of rigidity.

Blue et al [11] used a speaker to acoustically excite particles and piezoelectric ceramics in contact with these particles to measure the Density of Modes of airsoft pellets and corn in 3 dimensions. Their setup is shown in Figure 11 and results in Figure 12.

A Boson Peak is very noticeable as the Density of Modes measured deviates significantly from Debye scaling $D(\omega) \sim \omega^2$ in 3 dimensions.

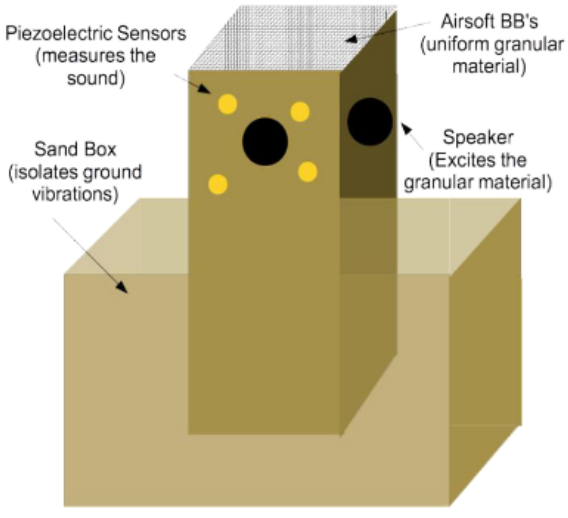

Figure 11: Blue et al [11] embed piezoelectric elements inside the walls of an isolated box with particles inside it and excite them with a speaker to measure the Density of Modes.

Blue [11] demonstrates the ability to accurately determine the Vibrational Density of Modes using piezoelectric ceramic sensors on acoustically vibrated particles. Then, we can calculate the Boson Peak using techniques by

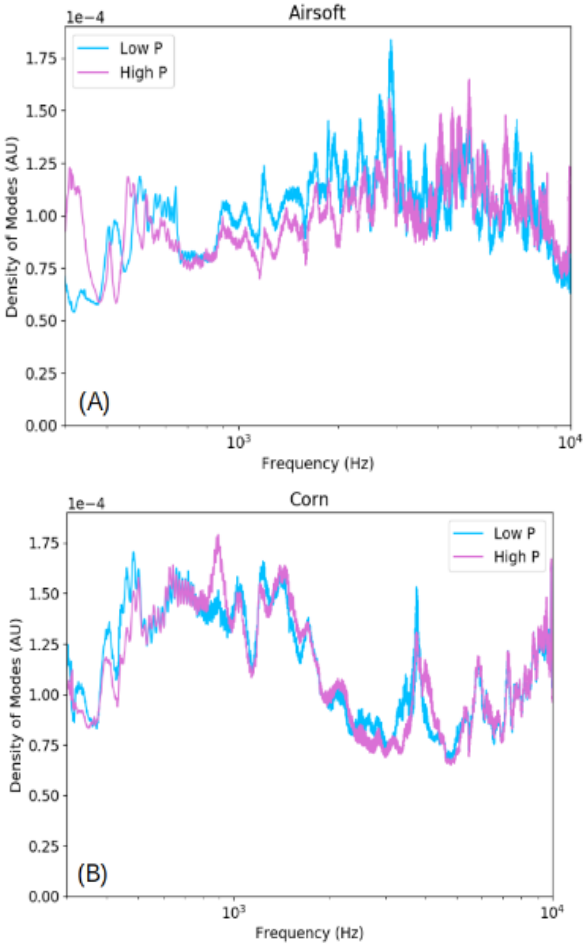

Figure 12: The Density of Modes measured using the setup in Figure 11 of (a) Airsoft pellets and (b) Corn [11].

Owens [9] like in Figure 9(c).

3. THE JAMMING TRANSITION

Disordered materials can flow like liquids when shaken, but they can also jam and gain rigidity if the shaking intensity is too high or too low. A liquid with low viscosity solidifies into a glass when the temperature is dropped rapidly preventing crystallization. A foam becomes rigid if stress is lowered and colloidal suspensions lose their ability to flow when the packing density is increased. In all of these cases, a different control parameter brings the disordered system into a controlled state without changing their structure.

Liu and Nagel [1] hypothesized a jamming phase diagram that explains many aspects of jamming in a system (Figure 13). Figure 13 exemplifies what universal factors cause jamming in disordered systems.

O'Hern et al [12] studied ideal spheres at zero temperature and zero shear stress. At low packing fraction Φ, particles are free to move around and flow like a fluid. As we increase the packing fraction, we eventually reach a critical value Φ_c, where the system jams and transitions

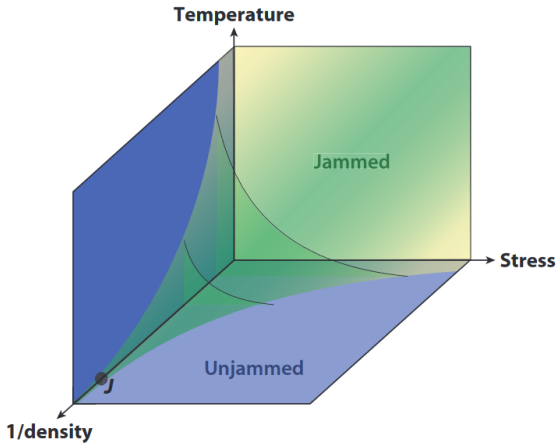

Figure 13: The jamming phase diagram. Outside the green area, a disordered system can flow, and inside, it remains jammed. This diagram captures the Jamming Transition of a system. The point J marks the jamming transition for ideal spheres at zero temperature and applied stress [10].

into a state where any infinitesimal force will be resisted by a force network between the spheres.

This critical value Φ_c is what Figure 14 captures. O'Hern describes multiple ways in which this jammed state achieved above the critical packing fraction is different from typical elastic solids and instead behaves similarly to low temperature glasses. This is why we see the jamming phase diagram shaped with a sharp discontinuity at J. At this critical point (J), O'Hern [12] showed that even slight increase in temperature caused low frequency modes to excite and cause the marginally jammed solid to lose rigidity. Similar observations were made for a slight increase in applied stress or a slight decrease in density.

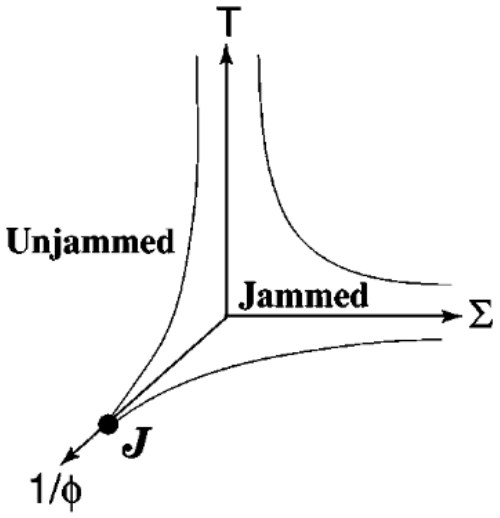

Figure 14: O'Hern et al measure the jamming transition point J where $\Phi = \Phi_c$ and the system transitions from order to complete disorder [12].

One of the most interesting results from O'Hern's work

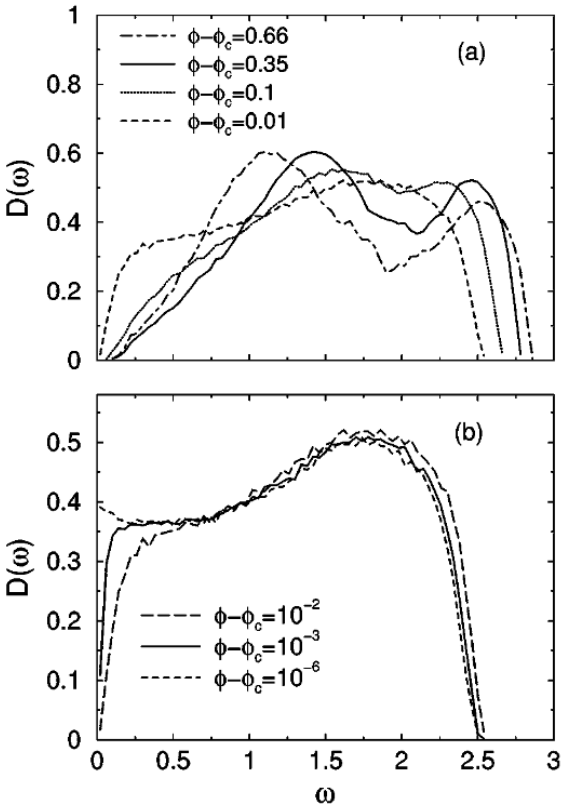

Figure 15: O'Hern et al measure the DoM for spherical glass beads with harmonic repulsions at zero temperature (a) far from Φ_c and (b) very close to Φ_c [12].

on the marginally jammed solid was his measurement of the Density of Modes near and around Φ_c (Figure 15). As a system approaches Φ_c, it develops an excess of low frequency modes as its Boson Peak located at ω^* drops lower and lower. As a marginally jammed system moves to become completely jammed (at Φ_c), we note $\omega^* \approx 0$. We observe this in Figure 14(b), where the Boson Peak moves to $\omega^* \approx 0$ as we move very close to Φ_c.

This is an exciting observation because we are now able to tell, from any plot of the Density of Modes, how jammed our system is, or how far it is from the jamming transition point J, just by looking for how far the value of ω^* is from $\omega = 0$ [12].

4. MOTIVATION IN GEOHAZARD FORECASTING

The main motivation for us measuring the change in ω^* as we approach a loss of rigidity is the applications in Geohazard forecasting. Geohazards like earthquakes and landslides are unpredictable- causing millions in property damage and injuring tens of thousands every year. Jerolmack and Daniels [13] explain how most geohazard-prone landscapes are composed primarily of soft matter in the sense that they are deformable and sensitive to collective effects. Landslides and earthquakes are both geohazards that affect our planetary landscapes, and are each informed by a loss of rigidity at a granular level which we can study by observing the rich dynamics of earth materials.

Jerolmack and Daniels explore the geophysical flow of different earth materials based on shear rate and packing fraction ϕ. They categorize geophysical flows into Soil Creep, Landslides, Debris Flow, Lahars and River Flows, Turbidity currents, Pyroclastic Density Currents and Fluid Muds; each associated with a different shear rate and ϕ. In this section, we aim to take a deeper look at Landslides and Earthquakes and the granular matter that informs each process.

4.1. Granular matter in Landslides

Jerolmack and Daniels [13] categorize geophysical flow of soft matter during landslides, which occur when wide layers of surface granular matter loses rigidity. They show that landslides occur in dry to partially wet systems with low packing fraction ϕ and higher shear than systems that demonstrate soil creep.

To demonstrate how landslides occur, Jaeger [2] collected a pile of mustard seeds as seen in Figure 16, and tilted them until the angle of repose θ. This is a simplified model of what occurs during a landslide.

In Figure 16, granular matter (a pile of mustard seeds) is tilted beyond the angle of repose, which causes slipping and a loss of rigidity at a surface, just like a landslide. As granular matter shifts in hilly regions, soil erosion and other factors change the angle of repose of the system until unjamming occurs at the surface. At this point, just like mustard seeds, the upper layers of soil experience a loss of rigidity and crumble as they flow downwards, causing a landslide- which is the primary example of a geohazard informed by granular failure at the surface.

4.2. Granular matter in Earthquakes

Earthquakes are more dynamic geohazards than landslides. Nevertheless, they too are caused by a loss of granular rigidity. In an earthquake, two tectonic plates (potentially kilometers wide) press into each other as they float on the mantle of the earth. At the point of contact, there is a fine collection of granular matter referred to as the fault gouge of the earthquake (potentially only a few millimeters thick). This gouge controls the movement of the tectonic plates and determines how the earthquakes vibrations are observed on the surface of the earth.

Johnson et al [14] used glass beads to simulate a "Laboratory Earthquake". The beads were used at the granular fault zone and were sheared under constant normal stress, along with perturbations from acoustics waves. They measured that with acoustic emissions, large failure events were disrupted in time, and often delayed by a cascade of smaller events, indicating a sort of strain memory in the granular material. Johnson's paper shows the direct impact of acoustic emissions on the granular matter in an earthquake effects its duration and time-span.

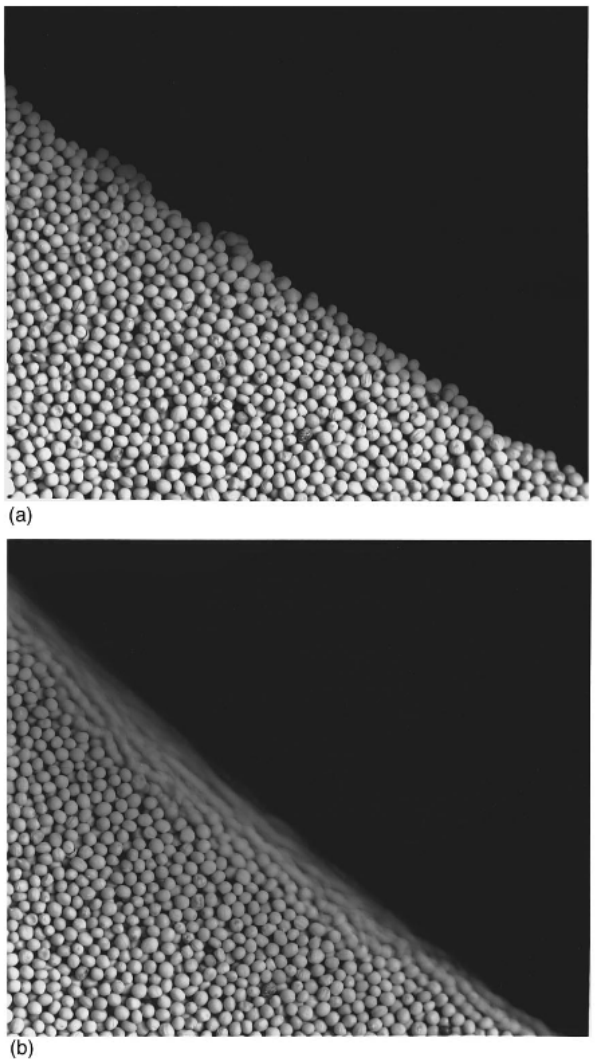

Figure 16: (a) A pile of mustard seeds tilted to an angle lower than the angle of repose θ. (b) Failure occurs after we increase the angle to be slightly greater than θ [2].

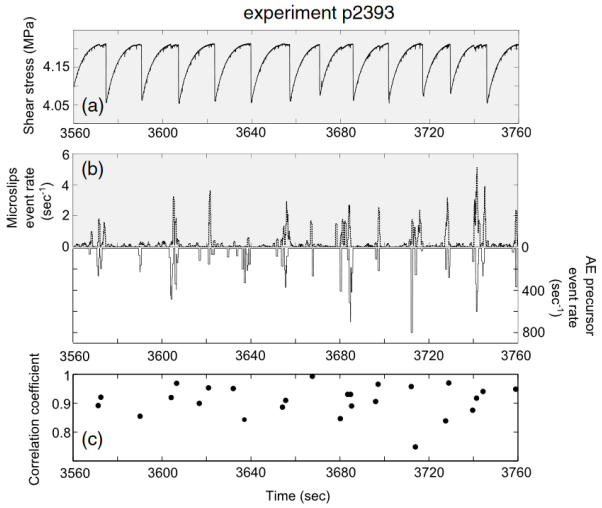

Figure 17: (a) Showing the shear stress signal from the experiment. (b) Showing the presence of microslip events during acoustic emissions. (c) Showing how the presence of microslip events correlate positively with stick-slip failure of the granular matter in the laboratory earthquake setup [15].

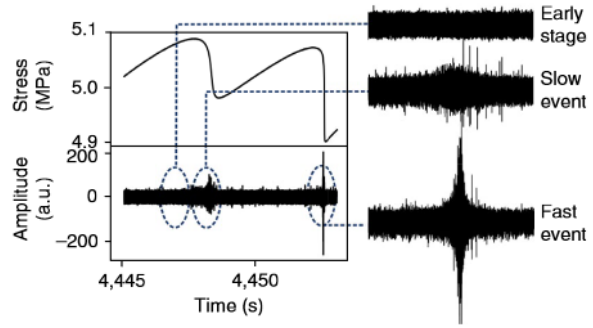

Figure 18: Showing how piezoelectric ceramics in contact with granular matter at the fault (in the gouge) were able to measure fast and slow laboratory earthquake events [16].

After noting that the granular matter in the gouge effects how and when earthquakes occur, Johnson followed up [15] by shearing glass beads above 3MPa and applying the same acoustic emissions. This time, they measured a series of micro-failure events that had an exponentially increasing rate of occurrence when the system was excited using acoustic emissions. The increase in micro-slip failure events eventually culminated in a larger stick-slip failure event (Figure 17 and Figure 18).

Six years later, Hubert [16] used machine learning to predict laboratory earthquake events (on sheared particles) using the fact that they are informed by granular failure at the fault. Much like Owens [9] and Brzinski [17] before them, they opted to use piezoelectric ceramics to measure the velocities of particles.

Using the series of voltages from the piezoelectric ceramics and their machine learning algorithm, Hubert et al were able to predict the timing and duration of laboratory earthquakes during shear of a quartz fault gouge under normal stress ranging from 1 to 10 MPa. Important aspects of this result are illustrated in Figure 19.

So, earthquakes duration, timing and size is likely related to the loss of rigidity at the fault and how granular matter behaves in the gouge. Using the piezoelectric voltages to perform a Density of Modes calculation and measuring how ω^* (or other similar low frequency features) change before, during and after an stick-slip failure event will likely tell us about how and why the loss of rigidity occurs.

5. RESEARCH QUESTION

To summarize this project's goals, first we will measure the Density of Modes of a granular sample using Dickey's method [18] (Explained in depth in Section 6.5), similar to how Owens [9] and Brzinski [17] have used it successfully in the past (with piezoelectric ceramics). Following Hubert's[16] observations using machine learning and Johnson's predictions [15] about granular matter inform-

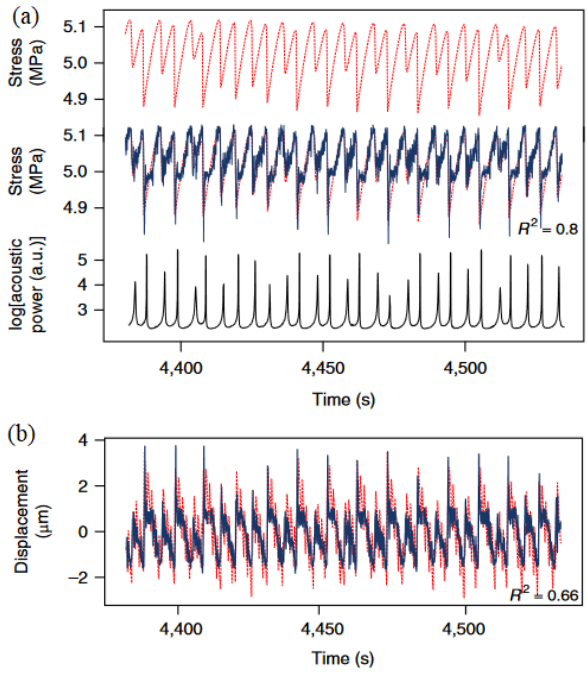

Figure 19: Hubert et al show their machine learning model predicting aspects of laboratory earthquakes with piezoelectric ceramics embedded in a quartz gouge. (a) Shows the stress and stick slip failure events in blue. (b) Shows the displacement of the piezoelectric elements in blue. In both figures, the red lines are predictions from the machine learning model, are accurate in predicting the timing and duration of stick-slip failure events [16].

ing a loss of rigidity in a system, we hope that the characteristic frequency ω^* of the boson peak or some other low frequency peaks in the DoM (or a related characterization of the shape of the DoM), when measured before an granular failure event, will allow us to forecast said event's beginning, duration or intensity.

More succinctly, can a measurement of the low frequency peaks in the Vibrational Density of Modes $D(\omega)$ of granular sample forecast geohazards that are characterized by a loss of granular rigidity?

6. INSTRUMENTATION AND METHODS

In order to measure the Density of Modes, we must measure the velocities of particles so we can apply our calculations. To do this, we will first discuss instrumentation that will be used to perturb and then extract velocity data from a sample of grains.

Before we can perform any measurements, we must extract a sample of grains from the earth with minimal disturbance to soil structure. To do so, we use a cylinder (24mm in length and 16mm in diameter) which we place perpendicular to the surface and push into the soil. To ensure that soil structure is preserved, the cylinders have a polished, beveled chisel-edge (Figure 20). Once the cylinder is embedded in the soil, we dig around it without touching the sample so as to not disturb the granular structure. Once the cylinder is easy to pull out, we use grain-tight caps on each end and seal the sample.

Figure 20: An image of the sample cylinders with bevelled edges containing a sample of collected soil.

With a sample collected, we can continue to a three step plan, through which we will measure the density of modes of the sample.

1. First, we apply a constant compressive strain to the sample from the top of the cylinder (See Section 6.1).
2. Secondly, we begin to acoustically excite the sample from the same end using a piezostack or a mechanical shaker (while keeping the sample under the compressive strain- See Section 6.2)
3. Finally, we use a piezoelectric ceramic of surface area 2MM × 2MM in contact with the grains to measure their velocities (See Sectin 6.3). From here, we apply a technique as described in [18] (see Section 6.5) in order to measure the Density of Modes.

6.1. Compressing samples and measuring pressure

Before we start mechanically driving our grains, we must design an apparatus that can apply sustained compressive strain that can be measured accurately, and keep this pressure constant as the sample is driven (Figure 21).

In the apparatus in Figure 21, a screw (marked in black) is guided to push an acrylic disk (yellow) into the top of the sample chamber (pink). The disk is made coupled to the grains using a thin layer of molasses (See Section 7.3), to ensure that it couples well with the sample. At the point where the screw and disk come in contact, a Force Sensing Resistor (red) is placed (FSR). This FSR is rated for 0.1-300 MPa with a response time of 1 ms.

When the screw is turned, it extends to push the acrylic disk into the sample chamber (upto 10mm), and thus the FSR experiences a force and outputs a resistance which can be measured using a circuit we designed (Figure 22). When unloaded, the FSR has an extremely high resistance($> 20M\Omega$), and as force is applied, it's resistance drops.

The circuit in Figure 22 is a simple non-inverting amplifier setup where the voltage measured at V_{OUT} is inversely

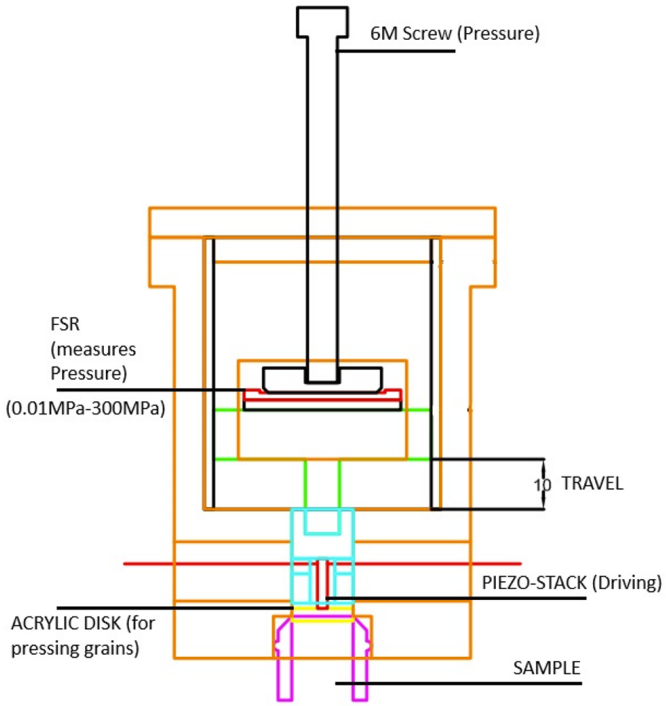

Figure 21: A schematic detailing how a sample of earth material placed under constant compressive strain. After this, the piezostack is activated and the sample can be driven with white noise or with a single frequency.

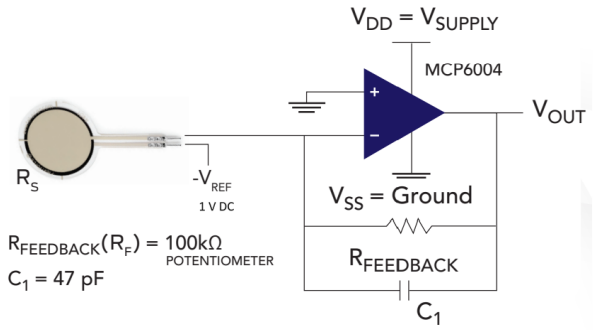

Figure 22: A circuit diagram detailing how to measure Force using an FSR [19].

proportional to the resistance of the FSR. As compressive strain is applied, the resistance drops and the gain of the amplifier increases ($|G| = |\frac{R_F}{R_{FSR}}|$), increasing the voltage output. So, we can now convert a force on the sample into a quantifiable voltage (See Section 7.1).

6.2. Acoustic Excitation with piezostacks

When the screw in Figure 21 is turned and the compressive strain is increased. This pushes the acrylic disk (yellow) and piezostack (red) into the chamber (pink). The stack can then be driven at any given frequency or with white noise. Figure 23 details the dimensions of this piezostack.

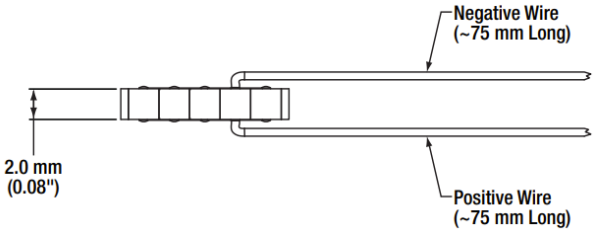

Figure 23: A detailed schematic of the piezostacks used to drive the sample as shown in Figure 21.

As mentioned above, the piezostack is coupled with the grains by placing a small acrylic disk between the two to distribute the vibrations along with a few drops of molasses as a couplant (See Section 7.3) used to ensure good contact between the sample and the stack.

6.3. Using piezoelectric ceramics to measure voltage

Now that we can apply compressive strain and mechanically drive our samples, we can turn our focus to measuring the DoM of the sample. This will be done using a separate piezoelectric ceramic coupled to the other end of the sample cylinder (Figure 25).

Piezoelectric ceramics have a crystalline structure that is deformable when force is applied. When deformed, the orientation of their crystalline lattice is squashed and thus causing an imbalance in the charge per unit area which causes a dipole vector to run through the crystalline lattice which one can measure as a voltage across the crystal (Figure 24).

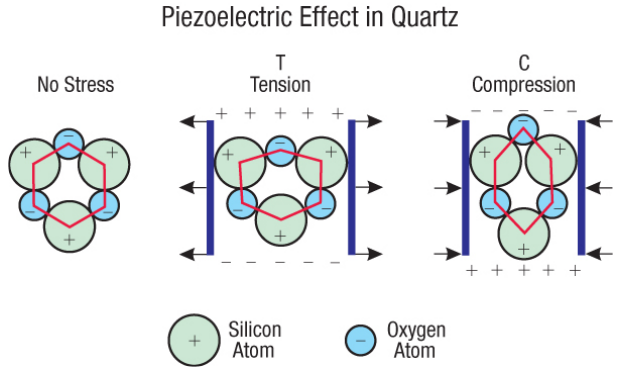

Figure 24: A diagram showing how piezoelectric ceramics produce a voltage [20].

The voltage produced by these ceramic structures is proportional to the force applied. Therefore, we can use their voltage as a method of measuring the force exerted on them by the particles in the chamber (and therefore their acceleration as particle mass stays constant.)

We couple a piezoelectric ceramic with a sample of grains as detailed in Figure 25. The ceramic is placed on a piston driven by a screw. It is then pushed 1 mm into the sample to ensure it is in contact with the grains. Using this ceramic, we can now measure a charge that

is proportional to the kinetic stress (acceleration) of the particles in contact with the ceramic.

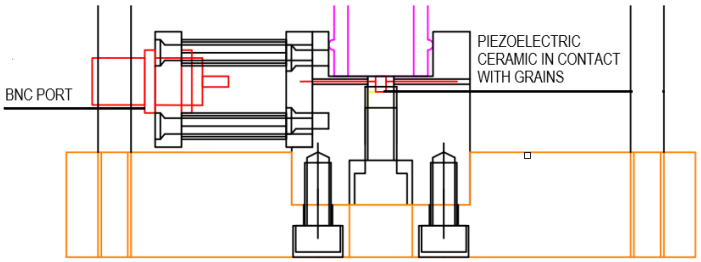

Figure 25: A schematic of the Piezoelectric ceramics are placed in contact with the grains as we extract voltage from the ceramics which is then passed through the instrumentation amplifier.

Now that we have a measure of the acceleration of the particles in the form of a charge from our piezoelectric ceramic, we must convert this into a reading of the Density of Modes. The piezoelectric ceramic has a surface area of 2mm × 2mm, so the charge produced is quite small and hard to work with. To make things simpler, we design an amplifier that will do a few things.

1. Firstly, we want our amplifier to convert this charge into a voltage.
2. Secondly, we want our amplifier to amplify the voltage to a more reasonable amplitude so we can manipulate it to find the DoM.
3. Finally, we do *not* want our amplifier to also amplify the noise on our signal, thus, we need a series of filters to get rid of this noise without changing the signal before we amplify.

To covert the charge from the piezoelectric ceramic into a voltage, we use a follower pre-amplifier (TLO72ACP). As detailed in Figure 26, this preamplifier contains 2 Op-Amps, which each connect to the two terminals of the ceramic. Consider the first terminal of the ceramic, which is connected to the positive terminal of the first Op-Amp (at Terminal 3 in Figure 26). We can measure the charge difference to ground by connecting our ground to Terminal 2 on Figure 26, and our output (Terminal 1) will be a voltage proportional to the charge on the piezoelectric ceramic. A similar process is carried out with Terminals 5, 6, and 7 to measure the total charge (as a voltage) across the piezoelectric ceramic.

Since the outputs of the TLO72ACP preamplifier will produce a voltage difference proportional to the charge difference on the two plates of the piezoelectric ceramic, the output is small, and therefore must be amplified so that we can apply our next components. We now amplify the signal while including a high pass filter at this Op-Amp to ensure the low frequency noise goes unamplified, so that we only amplify the signal and not the noise(Figure 28).

The first amplification circuit is a standard non-inverting amplifier circuit with a 10 MΩ resistor between Terminals 1 and 2 (and Terminals 6 and 7) of the follower,

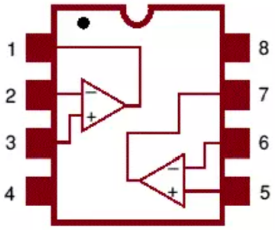

Figure 26: A circuit diagram detailing how the piezoelectric charge is converted into a voltage. Terminals 1, 2, and 3 are Op-Amp 1, Terminals 5, 6, and 7 are for Op-Amp 2, and Terminals 4 and 8 are for powering the Op-Amps with -15V and +15V respectively [21] [22].

and a 100Ω resistor between the piezoelectric ceramic and Terminal 2 (and 6). This should amplify our signal 10000 times. To filter low frequency noise, we can simply add a $1nF$ capacitor in parallel with each 10 MΩ resistor which creates a high-pass filter with $f_{3db} = \frac{1}{2\pi RC} = 16Hz$. It is also important to note that each side of the piezoelectric ceramic contains some charge, and therefore some capacitance (∼ 5 nF). Together with the two 100Ω resistors we attached to Terminals 2 and 6, these form high pass filters that form a high frequency cutoff.

Next, to further fine tune the high frequency cutoff, we add a parallel RL filter, using a 47Ω resistor and 1.2μH inductor in parallel on each output of the TLO72ACP (Terminals 1 and 7). The purpose of this filter is to reduce the interference between two consecutive taps to the piezo. This effect is called diffraction, as the two signals overlap and diffract similar to sound waves and primarly depends on the material and shape of the piezoelectric ceramic. Diffraction is often observed as a ringing/echoing effect on the output signal caused by the piezo and is fixed by dampening the relevant frequencies that cause the ringing therefore letting the signal reach ground faster after a force is applied to the ceramic. The $1.2\mu H$ inductor decides the high frequency cutoff past which frequencies are attenuated, and the 47Ω resistor decides how much attenuation is applied.

Finally, we pass the two outputs through a differential instrumentation amplifier- INA217 (Figure 27). This amplifier takes in the two signals (one positive and one negative) and amplifies them using the two Op-Amps labelled A1 and A2 in Figure 27. Then, these two signals are compared at the Op-Amp A3 and the difference is amplified further based on an external resistor ($1K\Omega$) with an gain of 10. Any common noise present in both lines is filtered out by the differential amplifier (as it does not appear in the difference measured by A3). Finally, we measure the output voltage against ground, and use it in Section 6.5 to calculate the Density of Modes of the sample.

6.4. Experimental Setup

Finally, the instrumentation in Sections 6.1, 6.2, and 6.3 is organized as shown in Figure 30 and the Density of Modes is calculated as the compressive strain (and there-

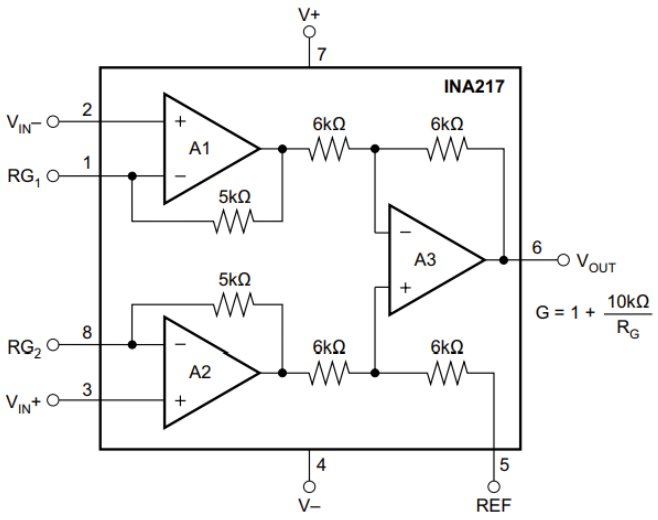

Figure 27: A circuit diagram detailing how an instrumentation amplifier works and provides common noise rejection [23].

fore pressure) is varied. The method (summarized below) will be applied to sands, clays, soils and other common earth materials.

1. The samples are placed under compressive strain and the pressure on the sample is noted using the FSR. Pressures range from 0.1 MPa to 300 MPa (see Section 6.1).

2. The samples are acoustically excited using the aforementioned piezostacks. White noise or single frequency noise are both supplied (see Section 6.2).

3. The piezoelectric ceramics in contact with the samples produce a charge proportional to the force applied to them. This force is proportional to the acceleration of the particles (see Section 6.3).

4. The amplifier we constructed converts the electric charge from the piezoelectric ceramics into a voltage which is measured as a vector using LABVIEW.

The next step is to calculate and plot the Density of Modes from the measured voltage.

6.5. Measuring the Density of Modes

The central technique we present in this paper is proposed by Dickey [18] used to measure the DoM of thermal systems from a series of velocities.

We have already seen how Owens [9] used piezoelectric elements in Figures 9, 11 and 12 to measure the change in ω^* with pressure. Brzinski and Daniels [17] use similar piezoelectric ceramics to measure a series of voltages proportional to the accelerations of the particles (Figure 29). In these two experiments, both Owens and Brzinski used Dickey's method[18] to measure the Density of Modes. This section will describe in detail how this method can be applied to calculate the Density of Modes and isolate the low frequency peaks like the Boson Peak.

Since the piezoelectric ceramics (Figures 9 and 29) provide a voltage V that is proportional to the force applied $F = ma$, we have:

$$V \propto a \tag{4.1}$$

We can perform an integral on the voltage V with respect to time, to create a vector that is proportional to the velocity of the particles.

$$\int V\,dt \propto v \tag{4.2}$$

Now, we apply Dickey's method, and use this vector of velocities v to calculate the Velocity Auto-correlation function with respect to a delay time τ.

$$C_v(\tau) = \frac{\sum_i \langle v_i(\tau + t) \cdot v_i(\tau)\rangle_\tau}{\sum_i \langle v_i(\tau) \cdot v_i(\tau)\rangle_\tau} \tag{4.3}$$

The Velocity Auto-Correlation function (VACF) correlates the velocity vector with itself over some delay time τ. This means that it compares the velocity at a point in time t to a point in time τ seconds ago, and marks the relative change for every single τ and t. Brzinski [17] and Owens [9] both use the VACF to compute a Fourier transform, whose real part gives the Vibrational Density of Modes $D(\omega)$.

$$D(\omega) = \int_0^\infty C_v(\tau) \cdot \cos(2\pi\omega t)\,d\tau \tag{4.4}$$

This technique was proposed for thermal systems, but Owens et al [9] (Figure 9) and Brzinski [17] (Figure 29) use piezoelectric ceramics to measure the acceleration of particles and then applied Dickey's thermal technique to measure the Density of Modes, thus demonstrating its effectiveness in athermal granular systems.

After we measure the Density of Modes, we divide by $\omega*^2$ (Debye scaling in 3D) to normalize the plot and isolate the low frequency peaks (like the Boson peak).

6.6. Systems

Following Section 6.1-6.5, we need to fit our compressive strain, acoustic driving and piezoelectric measurement systems together to read the Density of Modes. Figures 30-33 detail this process below and Figure 34 details how we link the systems up together.

Inside the experimental apparatus, we embed the FSR, Piezostack and Piezoelectric ceramic with their corresponding electronics.

Finally, we process the output from the Piezoelectric ceramic and calculate the Density of Modes.

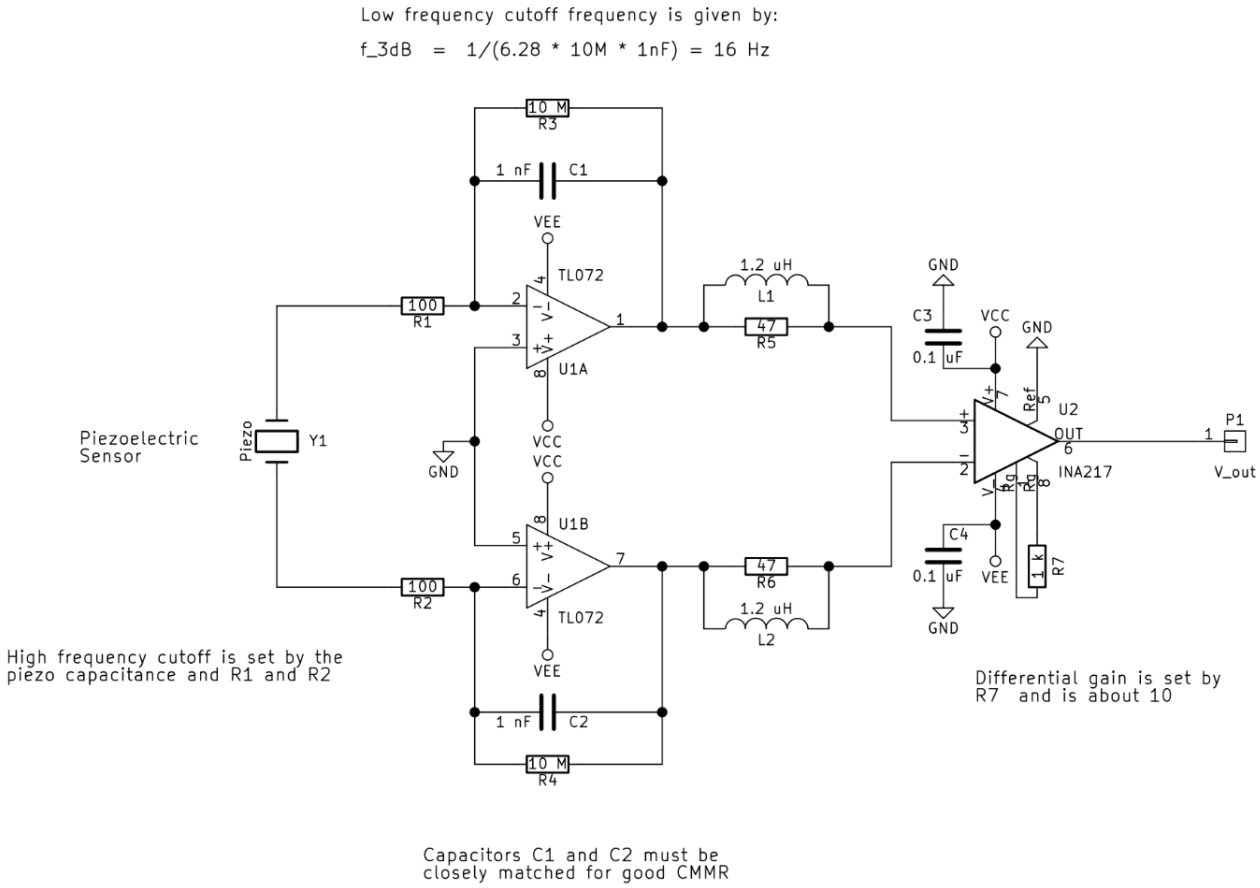

Figure 28: A circuit diagram of the final amplifier circuit [9] [+personal communication with Owens] used to convert the charge from the piezoelectric ceramic into a voltage and then amplify it into a readable signal to which we can apply Dickey's method from [18] (see Section 6.5).

7. CALIBRATION

After we have a working system, we need to calibrate different components to ensure that our readings are accurate and precise. Each of the 3 main measurements made by the system require calibration-

1. The voltage from the FSR circuit (V) needs to be translated into a force measurement (N).

2. We need to quantify what the expected response (mm/s) is for the piezostack surface for a given frequency (Hz) and input voltage (V).

3. We also need to quantify what the expected readout is from the piezoelectric ceramic (V) for a given frequency (Hz) and driving voltage (V).

7.1. Calibrating the FSRs

From Section 6.1 and Figure 33, we have a circuit outputs a voltage for a given force applied to the FSR. The compressive strain applied must be measured as a pressure on the sample cylinder- we need a calibration curve to do this. We apply a series of known forces[2] in increasing (inbound) and decreasing (outbound) by adding and removing weight to the FSR respectively. Then, we measure the output voltage through the circuit in Figure 33. This gives us a plot that we use to convert measured voltage into force (Figure 35).

The FSR voltage output creeps upwards when increasing the weight and downwards when decreasing it, leading to a hysteretic effect that grows as the time between measurements increases. This, ultimately, should not be a large problem so long as we calibrate the FSR with weights added at the same rate as we compress the samples, but this consideration must be included in the standard operating procedures for the apparatus.

7.2. Calibrating the Piezo-Stacks

Following Section 6.2, we need to quantify how the piezostack surface responds to a given voltage and a given frequency. The stack manufacturers provide the data for

[2] One can also use an Instron of choice if available.

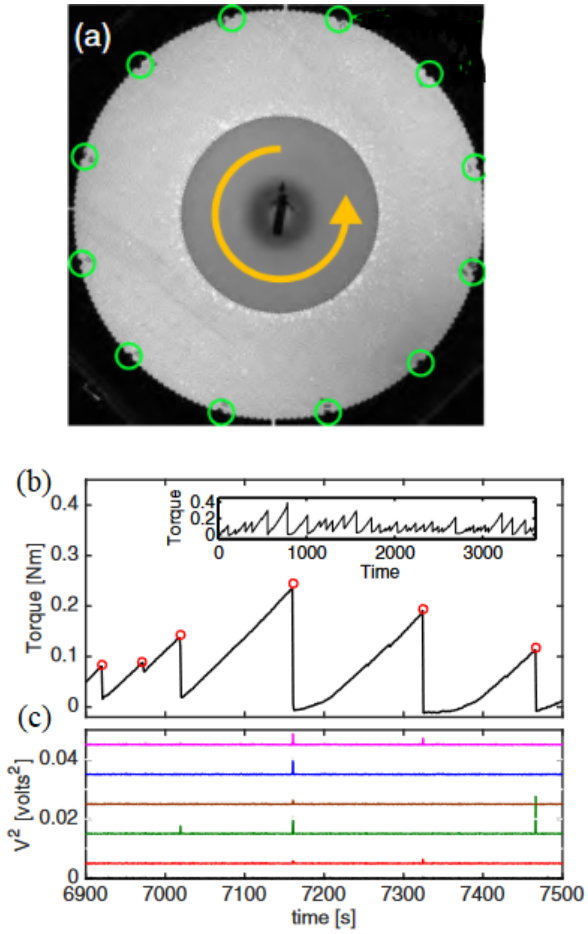

Figure 29: Brzinski et al [17] apply circular shear to granular matter in a cell with 12 piezoelectric ceramics embedded in the walls. (a) shows their setup. (b) shows details of the driving system and (c) shows clearly how slips in the granular matter appear on the voltage plots of the piezoelectric ceramics.

how much displacement to expect for a given driving voltage (Figure 36), which is important to for us to understand how both the stack and the ceramic respond to different input voltages.

We can drive the stack using a laser vibrometer at a variety of frequencies. We can insert the stack alone into the vibrometer and supply a range of frequencies (1Hz-25KHz) while measuring velocity at the top. Then, we can plot the velocity of the surface as measured by the vibrometer as a function of frequency below (Figure 37). This frequency response curve helps us understand how the stack responds to a given input frequency.[3]

An issue with using a small piezostack to drive a sample of grains has to do with the stack's comparatively small strain amplitudes. It is well understood that grains dissipate kinetic energy well [25], so a small perturbation will not be sensed by the piezoelectric ceramics on the other end. Additionally, if the piezostack is driven at a frequency too high or for too long, it will generate too much heat and burn up. This calibration curve (Figure 37) will allow us to better select driving frequencies so that we can achieve a higher driving velocity without burning out the stack.

7.3. Couplants

When providing acoustic perturbations to an amorphous sample, couplants are often used to provide an efficient path for sound to make its way to the surface of the sample. Air is a relatively poor conductor of sound, which means many different couplants are often used as a low-loss secondary transmission medium that is less dense than steel but more dense than air [26]. Couplants are also often used to fill in the irregularities in sample surfaces and provide a better contact for acoustic coupling [27] without disturbing the movement of the acoustic driver. There are many choices of viable couplants for most systems so we often choose one that is harmless and easy to apply smoothly and evenly and remove to the sample surface.

- **Water:** has a relatively high velocity and attenuation factor. This means that sound travelling through water has a high velocity, and a relatively hard time penetrating the surface of the medium (high attenuation). The attenuation factor is calculated by measuring the percentage of sound absorbed and scattered by the medium in question. Typically, when using water as a couplant, we add glycol to decrease the attenuation factor[4].

- **Glycerin:** has a very high velocity and attenuation factor almost like water. It also has a refractive index close to many plastics and metals so it can be used without the worry of bubbles distorting results. It is often used for studying concrete, brick and plastics.

- **Oil:** has the same velocity factor as water, but with lower attenuation than both glycerin and water. It is used to check surfaces that are difficult to immerse in liquids as oil is less dense.

- **Molasses:** is our choice of couplant for its ease of use and since members of our team are familiar with using it to study rock samples and other earth materials. It has a similar velocity and attenuation factor to glycerin and rarely forms bubbles.

Using a few drops of molasses to couple our piezostacks to the acoustic drivers will allow us to significantly improve the transmission of acoustic driving to the sample and improve our signal-to-noise ratio, which in turn leads to more accurate measurements.

[3] There are multiple maxima for each frequency bin in Figure 37 because we ran multiple sweeps to ensure that the stack output was not decaying as we ran the frequency sweep.

[4] At most 2 percent glycol- as more glycol causes bubbles which distort results significantly

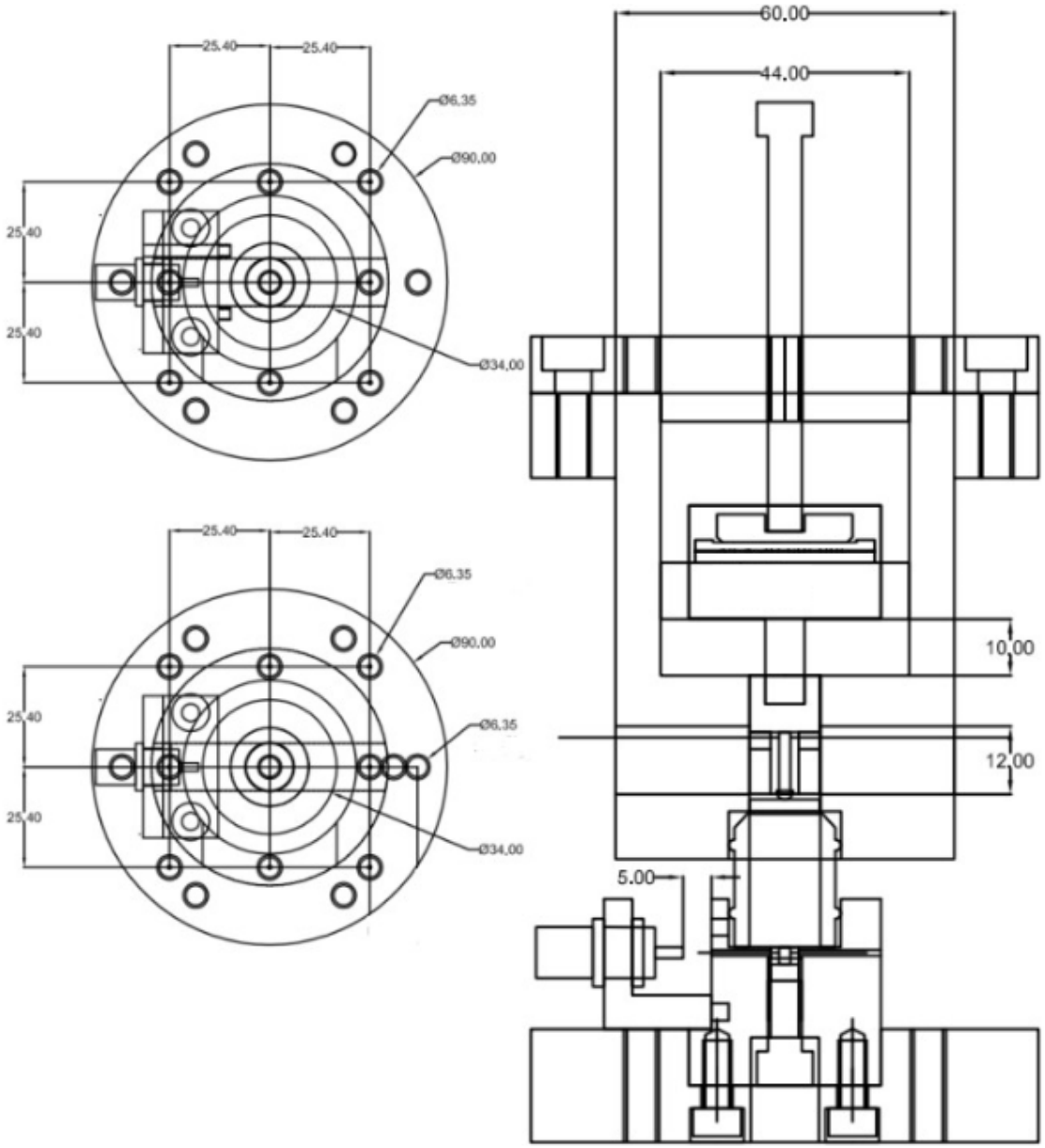

Figure 30: The schematics for the experimental apparatus.

7.4. Calibrating the Piezoelectric Ceramics- Future Calibration Work

Following Section 6.3, it is useful to quantify how our measurement piezoelectric ceramic responds to different frequency inputs. This process is similar to the process described in Section 7.2. We can drive the piezoelectric ceramic using vibrations from the piezostack. To do this, we need to couple the stack and the ceramic using a few drops of a couplant (mollasses) and then measure the output voltage using the PCB from Figure 33 for a given input frequency to the stack.

After measuring the output voltage, we need to account for the piezostack's response curve from Section 7.2, so we need to divide our voltage output by the data (velocities measured) in Figure 37 to obtain an accurate plot of voltage output vs input frequency.

We can repeat a similar process to measure the voltage response of the piezoelectric ceramic for a given voltage input to the piezoelectric stack. To do this, we need to measure the voltage output from the ceramic for a given voltage input provided to the stack, and then divide our data by the response (displacement measured) of the piezostack using Figure 36 to account for the stack's voltage response curve.

These two plots (frequency response and voltage response) should afford us a deep understanding of what frequencies and voltages we can expect our ceramics to measure particle accelerations well at, and therefore will allow us to select our driving frequencies and voltages appropriately.

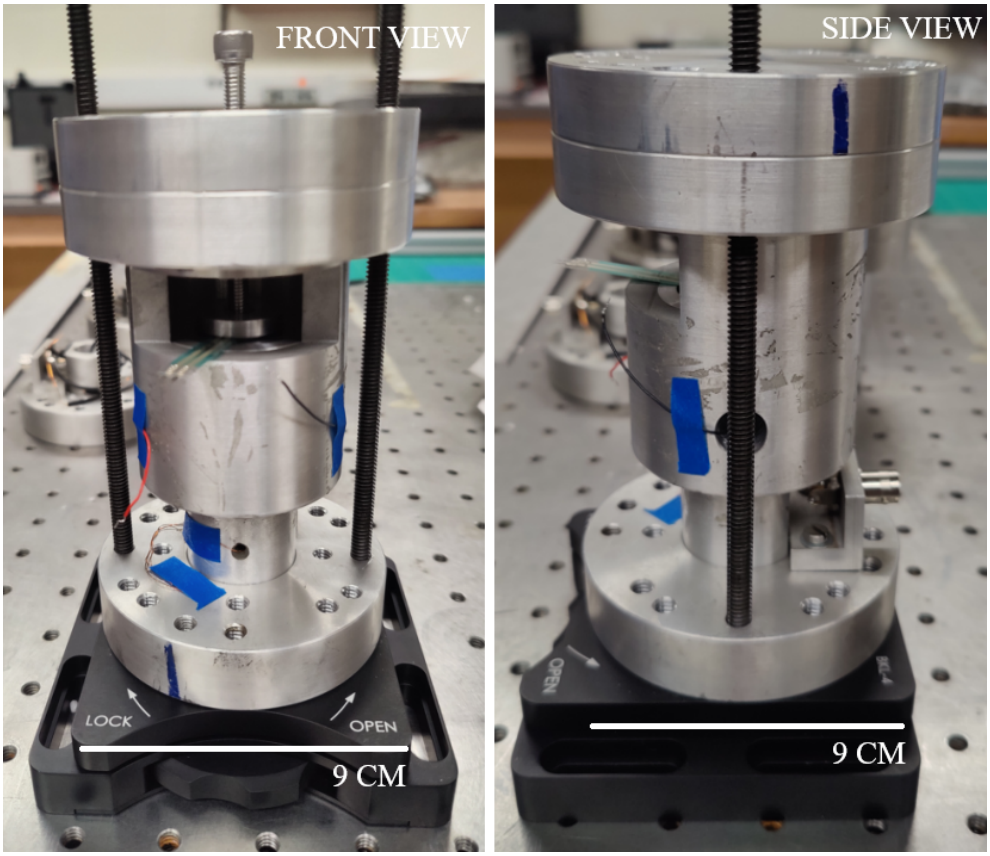

Figure 31: The experimental apparatus.

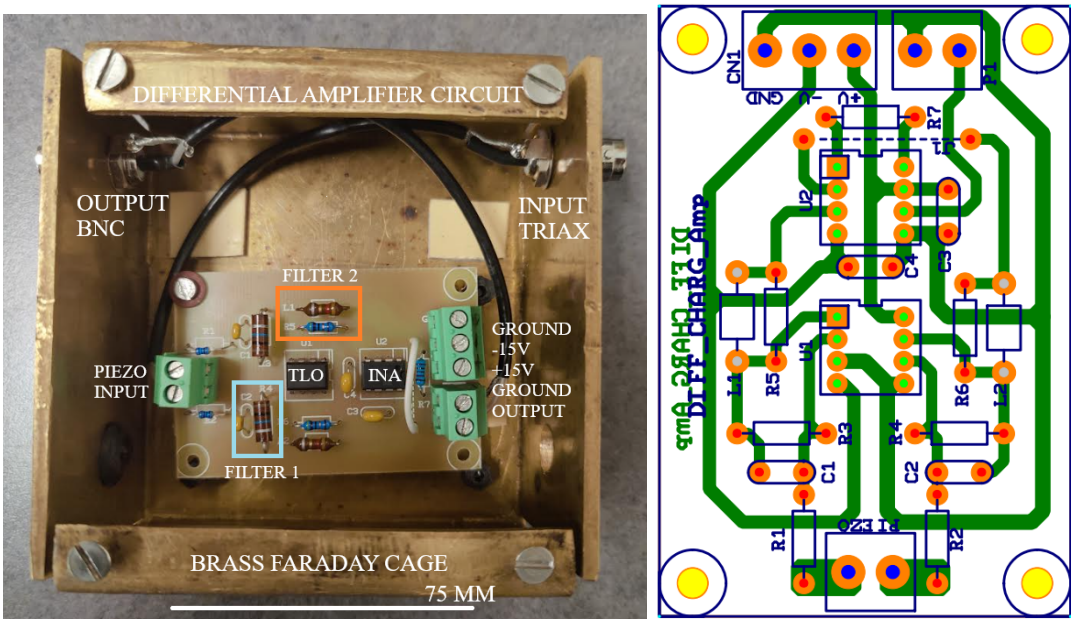

Figure 32: The shielded PCB from Figure 28 inside a brass faraday cage to protect from EMI.

8. DISCUSSION AND CONCLUSIONS

The instrumentation constructed and described in this thesis are built for 3 purposes. First, our apparatus can accurately measure and apply constant high amounts of compressive strain to amorphous earth materials on the order of 300MPa of pressure for a small sample cylinder (16mm Diameter x 24mm Height). Second, the apparatus can also drive and acoustically perturb the sample using a variety of waves or pulses supplied through an amplifier. Finally, using methods described by Dickey [18] and Owens et al [9] the piezoelectric ceramics (using an ampli-

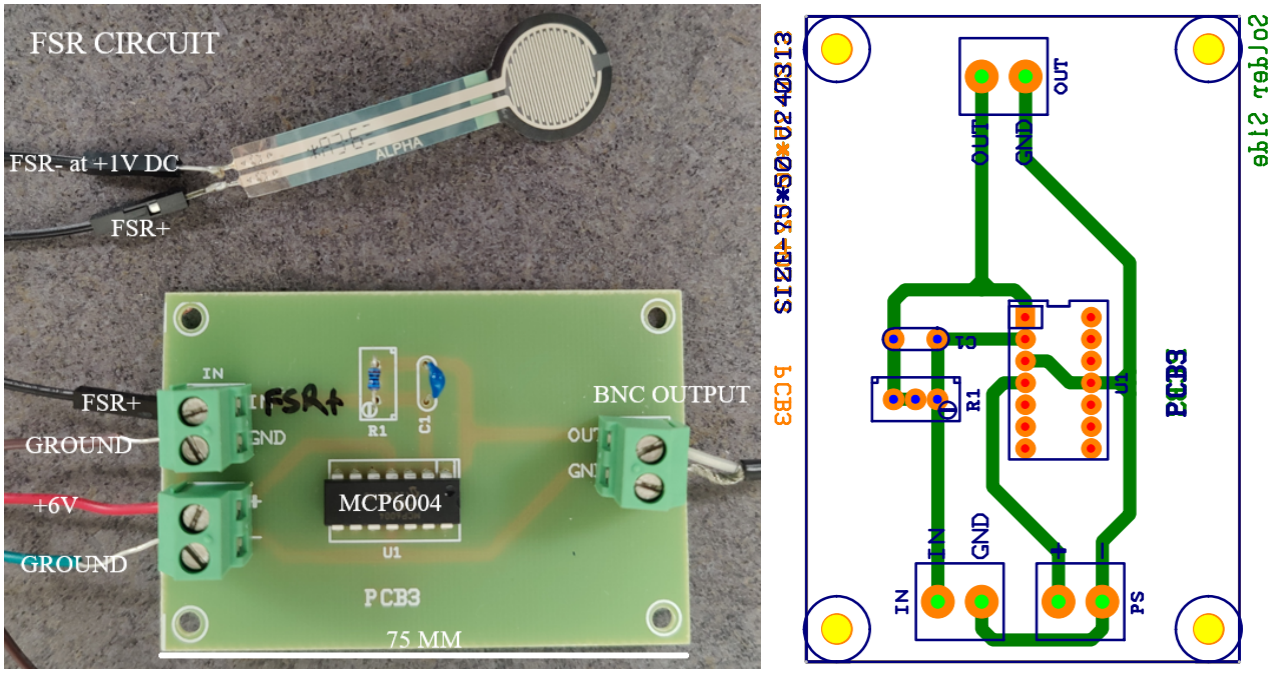

Figure 33: The PCB from Figure 22 used to measure the force from the FSR

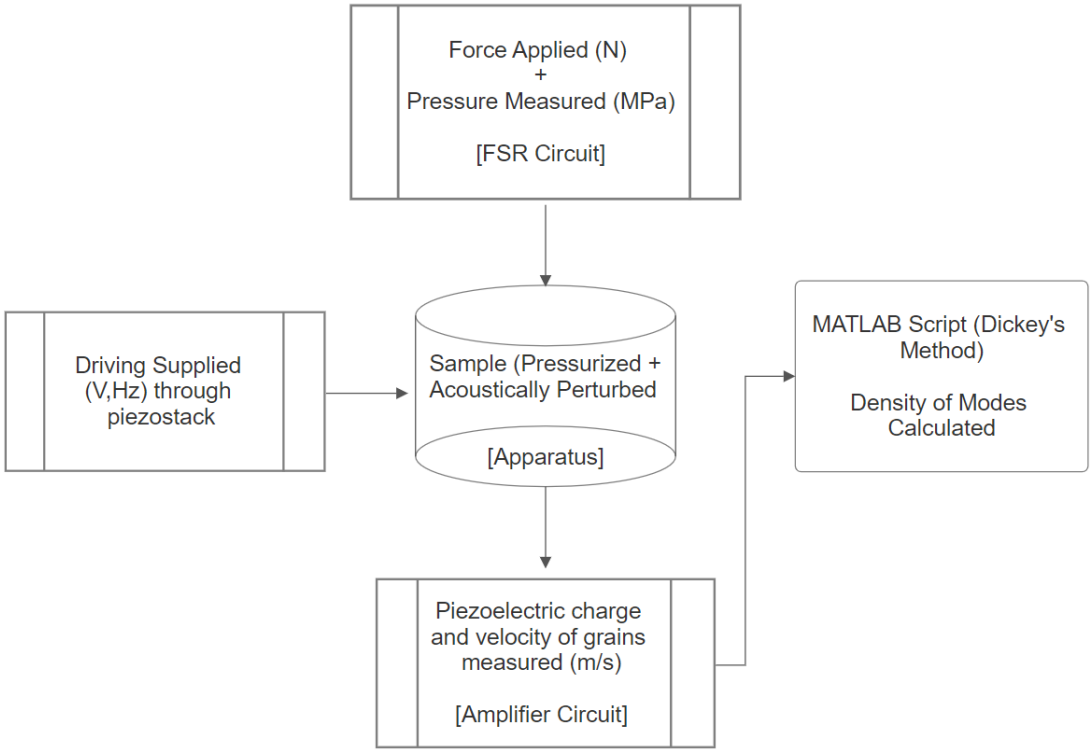

Figure 34: A flowchart of how the components shown in Figures 30, 32, and 33 function together.

fier and a script) allow for us to measure the velocities of particles and then calculate the Density of Modes of the sample of grains. We can then use this measurement of the Density of Modes to identify features (low frequency peaks like the Boson peak) that provide us with information about when the landscape (from where the sample was taken) might undergo a loss of rigidity.

A few pressing questions still remain. Now that the instrumentation is developed, how do we interpret readings from the piezoelectric ceramics? Additionally, what

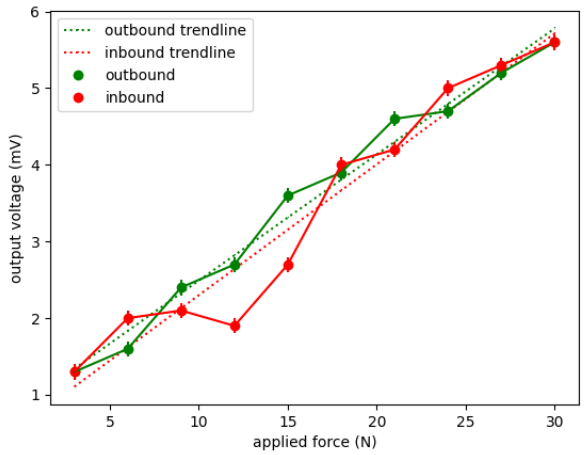

Figure 35: A force (N) v/s voltage (V) plot used to calibrate the FSR circuit.
[Special thanks to Clay Stoltenberg (Haverford) for help making this plot.]

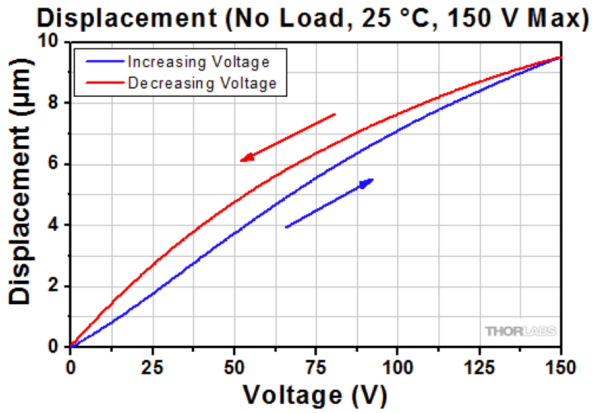

Figure 36: Thorlab's hysterisis curve for driving distance (μm) v/s input voltage (V) of the piezostack [24].

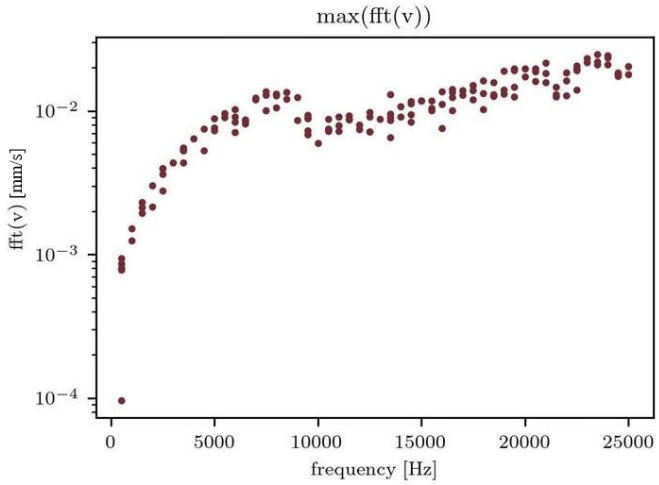

Figure 37: A laser vibrometer used to plot the input frequency (Hz) vs the surface velocity (mm/s) of the piezostack.
[Special thanks to Nakul Deshpande (NCSU) for help with this plot.]

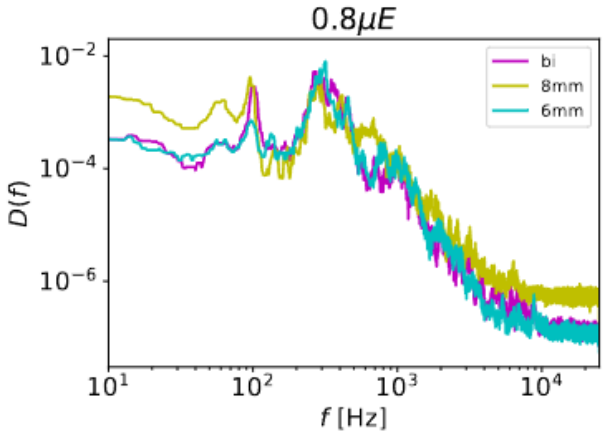

Figure 38: Owens et al [28] impact samples of grains of diameter 6mm, 8mm and a bidisperse packing with a pulse and use piezoelectric ceramics to measure the Density of Modes using Dickey's method. They note two consistent high wavelength (low frequency) peaks in the Density of Modes.

aspects of earth materials will this system tell us about?

8.1. Understanding the DoM measurement

A reading of the Density of Modes of a small sample of earth materials will not accurately represent the Density of Modes of the entire soil system, however, there are aspects of the sample that are relevant to the entire soil system. Owens et al [28] calculate the DoM using Dickey's method [18] and identify two distinct peaks of high wavelength (low frequency) modes (Figure 38).

The first of these peaks shown in Figure 38 occurs at a wavelength equal to twice the system length. The second, and more interesting peak seems to depend on the spacing between particles. In the DoM derivation (Section 2), we note that the wavelength of phonons depends on the interatomic spacing. Thus, in a granular system, Owens argues that the wavelength of the peak is dependent on spacing between grains and therefore increases under higher pressure when grains are packed tighter.[5] We hope to be able to use these low frequency peaks in the DoM to calibrate already existing geological monitoring software to detect when system might unjam.

Aspects of soil structure like packing fraction, particle shape and particle dynamics under constant compressive strain all affect the way the low frequency peaks shift as the sample approaches unjamming. We can quantify this

[5] It is important to note that as pressure is increased, the speed of sound in the grain packing changes, and this affects the relationship between the wavelength and frequency of a mode. This relationship is also characterized by Owens [28], and is used to analyze the frequencies of the peaks in the DoM using their phonon wavelengths.

failure in a set of samples by noting how the position of these peaks changes under pressure and acoustic perturbation. Then, we can use this information from the sample to forecast how the entire soil system might respond using Density of Modes measurements from seismographs and other geological monitoring software.

8.2. Future Work

In Sections 7.1 and 7.2, we calibrate the FSRs and piezostacks in order to quantify the measured force (with FSRs) and better understand how our piezostack responds to different driving frequencies and input voltages. The work from Section 7.2 will be extended to calibrate the Piezoelectric ceramic elements as described in Section 7.4. This will involve first plotting the voltage produced by the ceramic as a function of the input voltage provided to the stack coupled with the ceramic, and then plotting a frequency response curve by measuring the voltage output of the ceramic for a given frequency input to the coupled stack.

After the system is properly calibrated and the measurements made by the FSRs, piezostacks and piezoelectric ceramics are accurate, we will move on to measure the Density of Modes of the small sample cylinder and compare it with similar Density of Modes measurements from geophones embedded in the ground (taken while perturbing the soil). This way, we will be able to see what features of the Density of Modes of the entire landscape are captured in the Density of Modes of the small sample cylinder, and therefore what low frequency peaks we can use to potentially forecast unjamming in the broader system. The similarities and differences between the DoM of the landscape and the samples will provide us with crucial information about what aspects of the Density of Modes might inform a loss of rigidity and what features are simply a product of our measurement techniques. Extending Owens' [28] analysis from Section 8.1, a peak that is dependent on the size of the system (the sample cylinder) would not be so relevant to the landscape where the sample is extracted from, but a peak that is dependent on particle spacing can provide information about when a system of a particular grain size and structure might fail.

Owen's [28] also showed that pulses can be used in place of constant acoustic perturbation when measuring the Density of Modes. Pulses offer more consistency in amplitude and wavelength and can also be stronger- making obtaining a signal through a set of grains, which dampens forces well, much easier. In the coming months, we will modify our equipment (including the apparatus above) to provide not only constant acoustic perturbation, but also higher amplitude chirps (pulses). We can then compare the Density of Modes measured using a pulse versus a longer signal to confirm Owen's results. Stronger (higher amplitude) pulses will allow us to get signals through larger and looser packings of grains that dissipate forces well [25], and therefore will make our instrumentation more dynamic and applicable to a larger variety of granular systems.

The same system will also be used to further study the effects of acoustic perturbations on the structure of grain packings using tomographic scans at LBNL (μ-CTs). To do this, we will first place a sample under constant compressive strain, measure the Density of Modes, and take a μ-CT of the granular material. The resulting data (See Figure 39 for an example) offers detailed information on the full, 3-D structure of the material. After the initial scan, the sample will be acoustically perturbed and the Density of Modes will be remeasured, followed by a new μ-CT. The changes in Density of Modes and granular structure will allow us to better understand how our measurements can alter the state of earth material packings, whether structurally (μ-CT) or mechanically (acoustics).

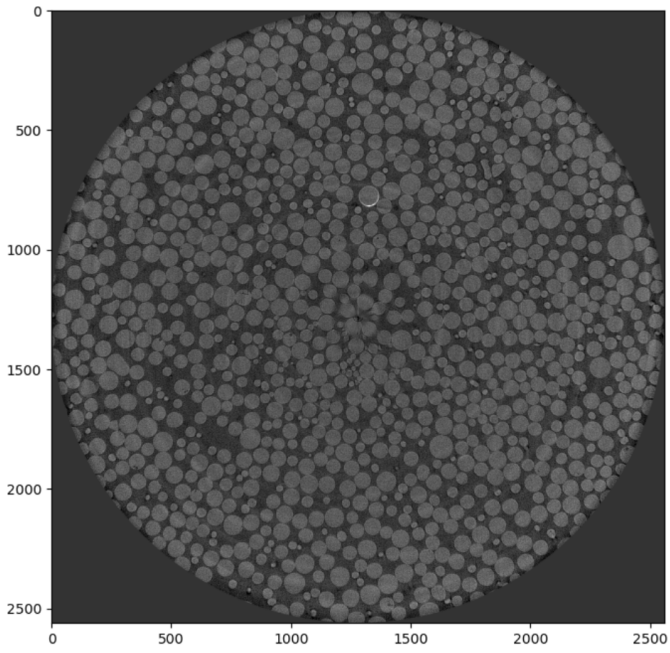

Figure 39: A tomography scan (1mm Diameter) of a layer of glass beads taken by us at LBNL in 2023.

Once we have identified the low frequency peaks in the Density of Modes that might inform failure in the landscape from where the sample was collected, we can apply computational methods like Hubert's laboratory earthquake models [16]. Using our understanding of how these peaks move as the system approaches failure, we can calibrate current geological monitoring instrumentation to detect when different types of earth materials might lose rigidity as described in Section 8.1.

9. ACKNOWLEDGMENTS

This project is a collaboration(NSF GLD-2244616) between Squishlab at Haverford, DanielsLab at NCSU and the Tectonorockphysics lab at the Scripps Institution of Oceanography (at UCSD). I would like to acknowledge Dr. Ted Brzinski, Dr. Karen Daniels, Dr. Vashan Wright, Dr. Nakul Deshpande and Richard Kilburn for helping me understand different aspects of the physics. Special thanks

to Leo Anderman and Clay Stoltenberg for their work on the project through 2023 and 2024. I would also like to thank Lawrence Berkeley National Laboratory for allowing our group to use their tomography facilities. Finally, I would like to thank Vijay Patki from EMag industries for helping me source materials and build instrumentation for this project.

[1] A. J. Liu and S. R. Nagel, Nature **396**, 21 (1998), ISSN 1476-4687, number: 6706 Publisher: Nature Publishing Group, URL https://www.nature.com/articles/23819.

[2] H. M. Jaeger, S. R. Nagel, and R. P. Behringer, Reviews of Modern Physics **68**, 1259 (1996), publisher: American Physical Society, URL https://link.aps.org/doi/10.1103/RevModPhys.68.1259.

[3] H. M. Jaeger, S. R. Nagel, and R. P. Behringer, Physics Today **49**, 32 (1996), ISSN 0031-9228, URL https://doi.org/10.1063/1.881494.

[4] J. B. Knight, H. M. Jaeger, and S. R. Nagel, Physical Review Letters **70**, 3728 (1993), publisher: American Physical Society, URL https://link.aps.org/doi/10.1103/PhysRevLett.70.3728.

[5] K. Stowe, Cambridge Unviersity Press **2** (2007).

[6] D. V. Schroeder and J. K. Pribram, American Journal of Physics **67**, 1284 (1999), ISSN 0002-9505, 1943-2909, URL https://pubs.aip.org/ajp/article/67/12/1284/1044922/An-Introduction-to-Thermal-Physics.

[7] N. Xu, M. Wyart, A. J. Liu, and S. R. Nagel, Physical Review Letters **98**, 175502 (2007), publisher: American Physical Society, URL https://link.aps.org/doi/10.1103/PhysRevLett.98.175502.

[8] K. Chen, W. G. Ellenbroek, Z. Zhang, D. T. N. Chen, P. J. Yunker, S. Henkes, C. Brito, O. Dauchot, W. van Saarloos, A. J. Liu, et al., Physical Review Letters **105**, 025501 (2010), publisher: American Physical Society, URL https://link.aps.org/doi/10.1103/PhysRevLett.105.025501.

[9] E. T. Owens and K. E. Daniels, Soft Matter **9**, 1214 (2013), publisher: Royal Society of Chemistry, URL https://pubs.rsc.org/en/content/articlelanding/2013/sm/c2sm27122b.

[10] A. J. Liu and S. R. Nagel, Annual Review of Condensed Matter Physics **1**, 347 (2010), _eprint: https://doi.org/10.1146/annurev-conmatphys-070909-104045, URL https://doi.org/10.1146/annurev-conmatphys-070909-104045.

[11] S. A. Blue and E. T. Owens (Presbyterian College, 2019), URL https://libjournals.unca.edu/ncur/wp-content/uploads/2021/02/2781-Blue-Sydney-FINAL.pdf.

[12] C. S. O'Hern, L. E. Silbert, A. J. Liu, and S. R. Nagel, Physical Review E **68**, 011306 (2003), publisher: American Physical Society, URL https://link.aps.org/doi/10.1103/PhysRevE.68.011306.

[13] D. J. Jerolmack and K. E. Daniels, Nature Reviews Physics **1**, 716 (2019), ISSN 2522-5820, number: 12 Publisher: Nature Publishing Group, URL https://www.nature.com/articles/s42254-019-0111-x.

[14] P. A. Johnson, H. Savage, M. Knuth, J. Gomberg, and C. Marone, Nature **451**, 57 (2008), ISSN 1476-4687, number: 7174 Publisher: Nature Publishing Group, URL https://www.nature.com/articles/nature06440.

[15] P. A. Johnson, B. Ferdowsi, B. M. Kaproth, M. Scuderi, M. Griffa, J. Carmeliet, R. A. Guyer, P.-Y. Le Bas, D. T. Trugman, and C. Marone, Geophysical Research Letters **40**, 5627 (2013), ISSN 1944-8007.

[16] C. Hulbert, B. Rouet-Leduc, P. A. Johnson, C. X. Ren, J. Rivière, D. C. Bolton, and C. Marone, Nature Geoscience **12**, 69 (2019), ISSN 1752-0908, number: 1 Publisher: Nature Publishing Group, URL https://www.nature.com/articles/s41561-018-0272-8.

[17] T. A. Brzinski and K. E. Daniels, Physical Review Letters **120**, 218003 (2018), publisher: American Physical Society, URL https://link.aps.org/doi/10.1103/PhysRevLett.120.218003.

[18] J. M. Dickey and A. Paskin, Physical Review **188**, 1407 (1969), publisher: American Physical Society, URL https://link.aps.org/doi/10.1103/PhysRev.188.1407.

[19] A. Industries, *Force Sensitive Resistor (FSR)* (2020), URL https://learn.adafruit.com/force-sensitive-resistor-fsr/overview.

[20] S. Technology, *Piezoelectric Material* (2020), URL https://www.audiowell.com/technology/186.html.

[21] Jotrin, *Exploring TL072 OP-AMP IC Pinout, Datasheet, Where & How to Use It - Jotrin Electronics* (2023), URL https://www.jotrin.com/technology/details/tl072-op-amp-ic-pinout-datasheet-use.

[22] M. Electronics, *TL072ACP Texas Instruments | Mouser* (2023), URL https://www.mouser.com/ProductDetail/Texas-Instruments/TL072ACP?qs=0OT4q4QBUTLFvIZ%252B%2FvrwoQ%3D%3D.

[23] T. Instruments, *INA217 data sheet, product information and support | TI.com* (2023), URL https://www.ti.com/product/INA217.

[24] Thorlabs, *Discrete Piezoelectric Stacks, 5.2 µm to 100.0 µm Travel* (2020), URL https://www.thorlabs.com/newgrouppage9.cfm?objectgroup_id=8040.

[25] M. N. Bannerman, J. E. Kollmer, A. Sack, M. Heckel, P. Mueller, and T. Pöschel, Physical Review E **84**, 011301 (2011), publisher: American Physical Society, URL https://link.aps.org/doi/10.1103/PhysRevE.84.011301.

[26] NDTkits, *Why we Need Couplant in Ultrasonic Testing?* (2021), URL https://ndt-kits.com/why-we-need-couplant-in-ultrasonic-testing/.

[27] P. Theobald, B. Zeqiri, and J. Avison (2008).

[28] S. A. Blue, S. C. Wright, and E. T. Owens, *Experimental Measurements of the Granular Density of Modes via Impact* (2024), arXiv:2403.10322 [cond-mat], URL http://arxiv.org/abs/2403.10322.